ADVANCED MATERIALS
www.advmat.de

A 3D Nitrogen-Doped Graphene/TiN Nanowires Composite as a Strong Polysulfide Anchor for Lithium–Sulfur Batteries with Enhanced Rate Performance and High Areal Capacity

Zhaohuai Li, Qiu He, Xu Xu, Yan Zhao, Xiaowei Liu, Cheng Zhou, Dong Ai, Lixue Xia, and Liqiang Mai**

Lithium–sulfur (Li–S) batteries have attracted remarkable attention due to their high theoretical capacity of 1675 mAh g^{-1}, rich resources, inexpensiveness, and environmental friendliness. However, the practical application of the Li–S battery is hindered by the shuttling of soluble lithium polysulfides (LiPSs) and slow redox reactions. Herein, a 3D nitrogen-doped graphene/titanium nitride nanowires (3DNG/TiN) composite is reported as a free-standing electrode for Li–S batteries. The highly porous conductive graphene network provides efficient pathways for both electrons and ions. TiN nanowires attached on the graphene sheets have a strong chemical anchor effect on the polysulfides, which is proved by the superior performance and by density functional theory calculations. As a result, the 3DNG/TiN cathode exhibits an initial capacity of 1510 mAh g^{-1} and the capacity remains at 1267 mAh g^{-1} after 100 cycles at 0.5 C. Even at 5 C, a capacity of 676 mAh g^{-1} is reached. With a high sulfur loading of 9.6 mg cm^{-2}, the 3DNG cathode achieves an ultrahigh areal capacity of 12.0 mAh cm^{-2} at a high current density of 8.03 mA cm^{-2}. This proposed unique structure gives a bright prospect in that high energy density and high power density can be achieved simultaneously for Li–S batteries.

With the growing demands for both high energy and power densities of energy devices, the lithium–sulfur (Li–S) battery has been considered as one of the candidates for the next generation batteries, which can deliver a significantly higher theoretical energy density (2600 Wh kg^{-1}) and a higher capacity (1675 mAh g^{-1}) than the traditional lithium-ion batteries (LIBs).[1,2] The practical application of Li–S batteries is however met with several technical challenges. For example, the insulating nature of sulfur and discharged products Li_2S/Li_2S_2 leads to low active material utilization efficiency. In addition, the severe dissolution of lithium polysulfides (LiPSs) into the electrolyte causes rapid capacity fading and low Coulombic efficiencies.[3,4] Moreover, a large volumetric expansion (80%) of sulfur during the charge–discharge process can cause collapse of the electrode structure, which is also a serious issue that should be considered in developing high-performance Li–S batteries.[5–8]

In the early stage, various kinds of nanostructured carbon materials have been explored to overcome a series of problems above.[9–14] While these structures and strategies can improve the performance of Li–S batteries, the suppression of the severe shuttling effect in these studies mainly utilized the physical interactions and the strength of the interactions is relatively weak.[15–17] More recently, many groups adopted transition metal oxides as the polar sulfur hosts, which have been demonstrated to possess strong chemical binding to LiPSs.[18–20] Cui and co-workers[21] designed and prepared S/TiO_2 yolk–shell nanostructure as a cathode to inhibit the dissolution of LiPSs, which achieved an initial capacity of 1030 mAh g^{-1} at 0.5 C and displayed good stability. Liang and Nazar[22] reported a structure of MnO_2 nanosheets decorated sulfur particles with sulfur as the core and MnO_2 as the shell. A high capacity of 950 mAh g^{-1} was remained after 300 cycles at 0.5 C, which is due to the strong absorption between polar MnO_2 and LiPSs. However, metal oxides with intrinsic low electric conductivity will ultimately impede the electron transport and interrupt the movement paths for Li ions, causing slow electrochemical reaction rates and thus leading to poor rate capability.

Compared to metal oxide, transition metal nitrides (TMNs) have higher conductivity and chemical stability, which have been employed as anchoring materials for LiPSs recently.[23–33] Due to the high theoretical electrical conductivity of titanium nitride,

Z. H. Li, Dr. X. Xu, X. W. Liu, C. Zhou, L. X. Xia, Prof. L. Q. Mai
State Key Laboratory of Advanced Technology for Materials Synthesis and Processing
International School of Materials Science and Engineering
Wuhan University of Technology
Hubei, Wuhan 430070, P. R. China
E-mail: xuxu@whut.edu.cn; mlq518@whut.edu.cn
Q. He, Prof. Y. Zhao
State Key Laboratory of Silicate Materials for Architectures
International School of Materials Science and Engineering
Wuhan University of Technology
Hubei, Wuhan 430070, P. R. China
D. Ai
School of Mechanical and Electronic Engineering
Wuhan University of Technology
Hubei, Wuhan 430070, P. R. China
The ORCID identification number(s) for the author(s) of this article can be found under https://doi.org/10.1002/adma.201804089.

DOI: 10.1002/adma.201804089

Cui and co-workers[28] reported a titanium nitride-enabled stable Li–S battery (TiN-S), which showed capacity decay of only 0.07% per cycle over 500 charge/discharge cycles. Kim and co-workers[29] reported that the heterogeneous catalytical sites on TiN can strongly interact with the LiPSs and spatially confine them near the electrode surfaces, preventing the shuttle effects more aggressively.

Herein, we constructed a 3D nitrogen-doped graphene/TiN nanowires composite (3DNG/TiN) as a freestanding electrode for Li–S batteries. The schematic of the fabrication process of 3DNG/TiN is shown in **Figure 1**a. First, $H_2Ti_3O_7$ nanowires (Figure S1a–c, Supporting Information) were dispersed in aqueous graphene oxide (GO) suspension. The formation of 3DG/$H_2Ti_3O_7$ composite (Figure S1d–f, Supporting Information) was induced by introducing the sodium ascorbate to reduce GO and conjugate the reduced GO (rGO) into the 3D hydrogel. 3DNG/TiN was obtained by annealing the 3DG/$H_2Ti_3O_7$ aerogel in NH_3 atmosphere. Without any conductive additives or binders, the 3D porous graphene framework can provide the superb electron and ion transport pathways. The TiN nanowires on the graphene nanosheets have strong chemical absorptivity of LiPSs, which can anchor LiPSs on the

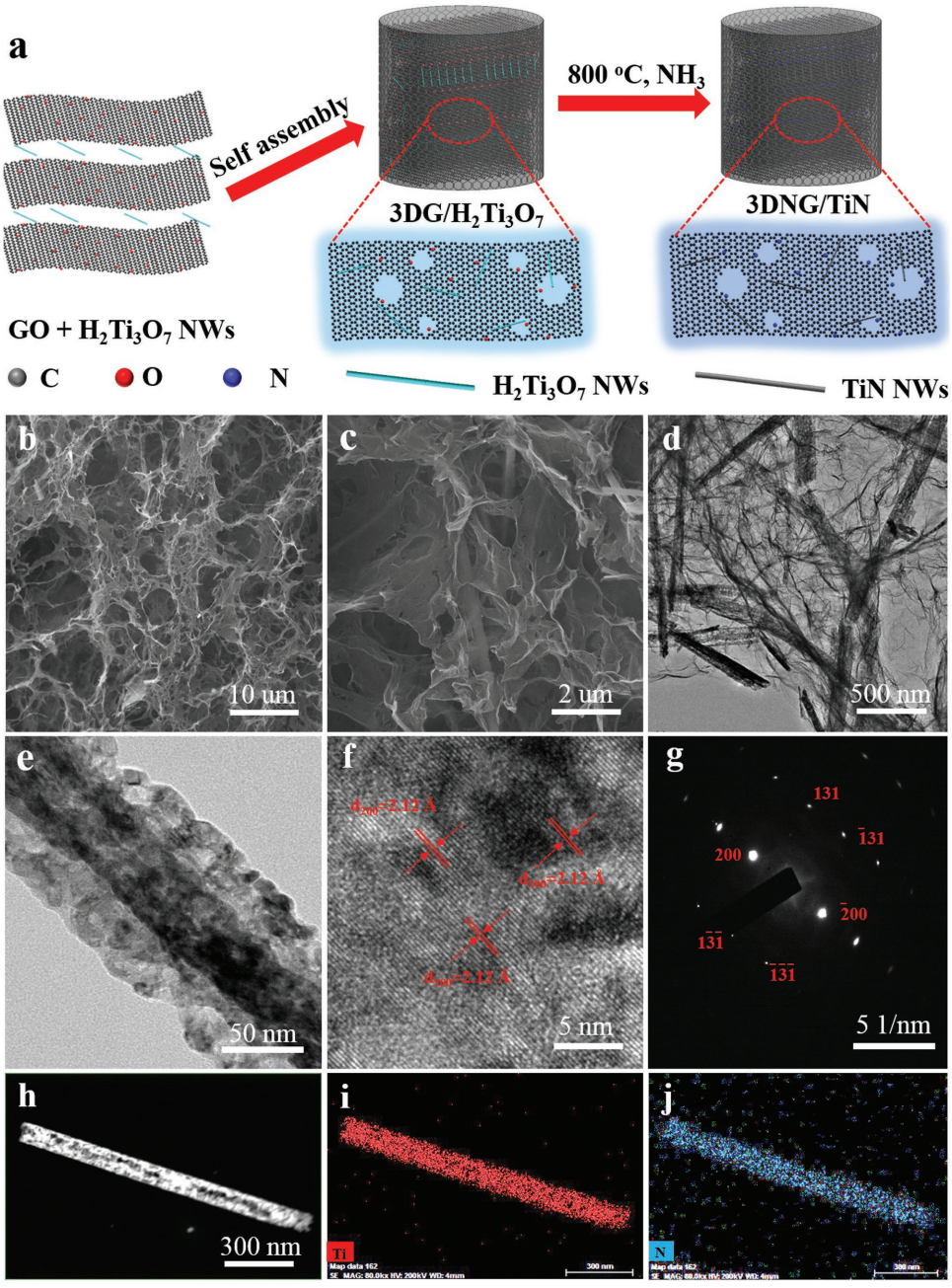

Figure 1. Schematic of the fabrication, morphology and structural characterization of the 3DNG/TiN. a) Schematic, b,c) SEM images, d,e) TEM images, f) High-resolution TEM (HRTEM) image, g) SAED pattern, and h–j) TEM elemental mapping images.

surface and promote the conversion between the long-chain and short-chain LiPSs.

Figure 1b,c show that 3DNG/TiN have a 3D interconnected network with a large number of microsized voids, which are able to carry sufficient sulfur to achieve high sulfur mass loading and accommodate the electrochemically derived volume changes. TiN nanowires are uniformly dispersed in the graphene framework, which is further confirmed by elemental mappings of Ti, N, C, and O in 3DNG/TiN (Figure S2, Supporting Information). From the transmission electron microscopy (TEM) image in Figure 1d, the single-dispersed TiN nanowires tightly attached on the wrinkled graphene nanosheet are observed. In contrast, TiN nanowires obtained without the supporting of graphene framework (Figure S3, Supporting Information) show serious aggregation, which indicates that graphene nanosheets can effectively maintain the good dispersion and localization of the TiN nanowires. After the gas generation and recrystallization during the annealing process, the surfaces of TiN nanowire become coarse and contain many nanosized holes (Figure 1e), which is due to the vacancies created during the anion exchange and phase transformation processes. The Barrett–Joyner–Halenda (BJH) pore size distribution curves of TiN nanowires are shown in Figure S4 in the Supporting Information. The pore sizes of TiN nanowires are mainly below 20 nm and the specific area is 65.55 m^2 g^{-1}, which can improve the contact between polysulfides and TiN, and enhance the adsorption of polysulfides. The HRTEM image (Figure 1f) of the TiN nanowire shows distinct lattice fringes with a *d*-spacing of 2.12 Å, corresponding to the (200) plane of the highly crystallized TiN.[34] The result is in accordance with the SAED pattern, which is a typical single crystal diffraction pattern with striking diffraction points of TiN lattice planes (Figure 1g). The TEM elemental mappings (Figure 1h–j) further show a uniform distribution of titanium and nitrogen in a single TiN nanowire.

Figure 2a shows the X-ray diffraction (XRD) patterns of the pure $H_2Ti_3O_7$ nanowires, TiN nanowires, and 3DNG/TiN, demonstrating the successful transformation from $H_2Ti_3O_7$ to TiN phase both with and without rGO. The diffraction peaks of the TiN nanowires correspond to the standard NASICON phase of TiN (JCPDS card No. 87–0632). The mass percentage of TiN nanowires in 3DNG/TiN is found to be 31.5% by thermo gravimetric analysis (TGA) as shown in Figure 2b. This reasonable content of the TiN nanowires not only guarantees the anchoring of LiPSs, but also ensures the proper weight of the entire working electrode to obtain a high energy and power densities of the battery.

Coin cells were assembled to test the electrochemical performance of 3DNG/TiN. The Li_2S_6 catholyte was added to 3DNG/TiN as the cathode during the cell assembly. 3DG/TiO_2 and 3DNG cathodes were also prepared for the comparison. The initial four cyclic voltammetry (CV) curves of 3DNG/TiN cathode (**Figure 3**a) show no obvious peak shifts or current changes, demonstrating the good reversibility of such electrochemical system with 3DNG/TiN. The two reduction peaks locate at 2.31 and 1.98 V, which are known to be the electrochemical transformation from soluble long-chain LiPSs to short-chain LiPSs and then to insoluble discharge products Li_2S_2 and Li_2S. In the charge stage, the oxidation peak around 2.45 V is due to the conversion of Li_2S (Li_2S to Li_2S_8 and then to sulfur).[35,36] Figure S5a (Supporting Information) presents the initial CV profiles of 3DNG/TiN, 3DG/TiO_2, and 3DNG cathodes, it is obvious that the reduction peaks of the 3DNG/TiN cathode appear at higher potentials than those of the 3DG/TiO_2 and the 3DNG cathodes. The distinguishable move of both oxidation and reduction peaks of the 3DNG/TiN cathode indicates the improved polysulfide redox kinetics by the TiN nanowires.

The cycling performance of 3DNG/TiN, 3DG/TiO_2, and 3DNG at 0.5 C were evaluated as shown in Figure 3b. The areal sulfur loading of the three electrodes is 4.8 mg cm^{-2}. The 3DNG/TiN cathode delivered an initial discharge capacity of 1510 mAh g^{-1}, and a high capacity of 1267 mAh g^{-1} was retained after 100 cycles, indicating that the dissolution of LiPSs into organic electrolyte was effectively restrained by the 3DNG/TiN electrode. By contrast, 3DG/TiO_2 and 3DNG cathodes delivered initial discharge capacities of 1268 and 1402 mAh g^{-1}, respectively. After 100 cycles, the capacities decreased to 923 and 817 mAh g^{-1}, respectively, implying the severe dissolution of the polysulfide with low sulfur utilization. To elucidate whether 3DNG/TiN provides extra capacity during the discharge process, the electrochemical reactivity of 3DNG/TiN was tested between 1.6 and 2.8 V without Li_2S_6 catholyte at the current density of 0.5 C (Figure S6, Supporting Information). It is noted that the first discharge capacity of 3DNG/TiN is 32 mAh g^{-1}, and the capacity remains only 3.8 mAh g^{-1} after 100 cycles, which is negligible. The galvanostatic charge/discharge curves of 3DNG/TiN cathode at different cycles are shown in Figure S5b in the Supporting Information. The shape of the profiles does

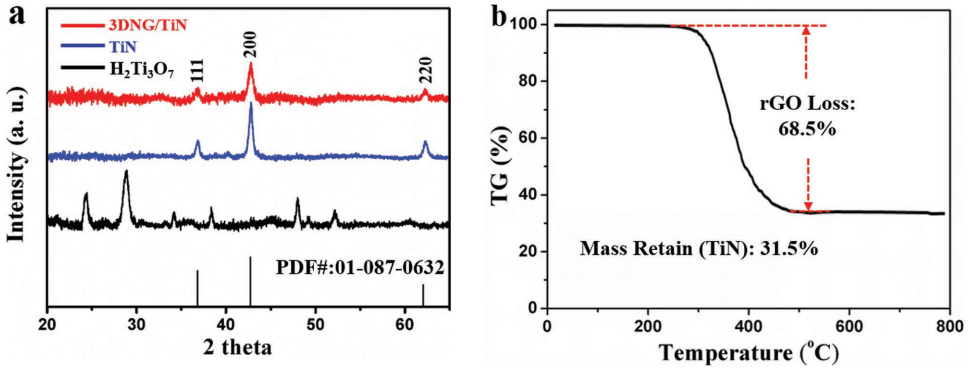

Figure 2. a) XRD patterns of the $H_2Ti_3O_7$, TiN, and 3DNG/TiN. b) TG curve of the 3DNG/TiN composite.

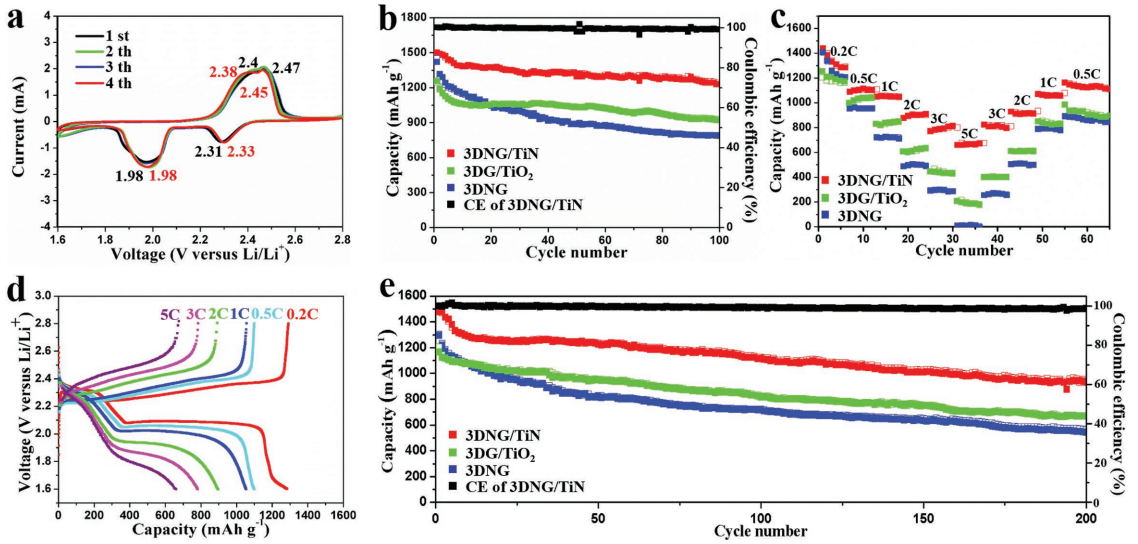

Figure 3. Electrochemical performances of 3DNG/TiN, 3DG/TiO_2, and 3DNG cathodes. a) CV profiles of the 3DNG/TiN at a scan rate of 0.1 mV s^{-1}. b) Cycling performance of the 3DNG/TiN, 3DG/TiO_2, and 3DNG cathodes at 0.5 C for 100 cycles. c) Rate performance of the 3DNG/TiN, 3DG/TiO_2, and 3DNG cathodes. d) Galvanostatic charge–discharge profiles of the 3DNG/TiN at different rates in a potential window from 1.6 to 2.8 V. e) Cycling stability of the 3DNG/TiN, 3DG/TiO_2, and 3DNG cathodes at 1 C for 200 cycles.

not change obviously from the 1st to the 100th cycle and two discharge plateaus and one charge plateau are observed in each cycle, indicating a stable electrochemical behavior of the 3DNG/TiN cathode. In order to determine a proper content of TiN in the composite and thus guarantee an optimal configuration of high energy density and good cycling stability, the cycling performance of the 3DNG/TiN with different contents of TiN (31.5, 25.5, and 20.2 wt%) at 0.5 C are shown in Figure S7 in the Supporting Information. It is clearly that the 3DNG/TiN with 31.5 wt% of TiN has the best performance, which means it is a suitable content to guarantee the anchoring of LiPSs and ensure the proper weight of the entire working electrode to obtain high energy and power densities of the battery. To further confirm the positive effect of TiN nanowires, the first galvanostatic charge/discharge curves of the 3DNG/TiN, 3DG/TiO_2, and 3DNG are compared in Figure S5c in the Supporting Information. The discharge plateaus of 3DNG/TiN are longer and flatter with a higher capacity and a lower polarization ($\eta = 0.24$ V) than 3DG/TiO_2 ($\eta = 0.35$ V) and 3DNG ($\eta = 0.42$ V) electrodes, suggesting a kinetically enhanced reaction process of 3DNG/TiN.

The rate capabilities of the three cathodes were further investigated at various current densities from 0.2 C to 0.5 C, 1 C, 2 C, 3 C, and 5 C, and the corresponding average reversible capacities were 1327, 1090, 900, 789, and 676 mAh g^{-1}, respectively (Figure 3c). After the high rate cycling, a high specific discharge capacity of 1134 mAh g^{-1} was recovered at 0.5 C. The 3DG/TiO_2 and 3DNG cathodes showed comparable capacities at low current densities. However, the capacity gaps between these two cathodes and 3DNG/TiN increased with the current density increase, and the capacities of only 192 and 25 mAh g^{-1} were remained for 3DG/TiO_2 and 3DNG at 5 C, respectively. The galvanostatic charge/discharge curves of the 3DNG/TiN at different rates are shown in Figure 3d. Although the polarization occurred in the electrodes at higher rate due to slower dynamics of sulfur, all the profiles consist of two discharge plateaus. The electrochemical impedance spectroscopic (EIS) test of 3DNG/TiN cathode at different cycles is shown in Figure S5d in the Supporting Information. It is obvious that the resistance (R_{ct}) of the cells becomes smaller after cycling and remains at a stable value (11–16 Ω), indicating an excellent electronic conductivity and the stable electrochemical reactions. Moreover, The 3DNG/TiN cathode has a smaller charge transfer resistance (20 Ω) than that of the 3DG/TiO_2 (38 Ω) and 3DNG cathodes (24 Ω), which can be explained by enhanced interfacial affinity between TiN and LiPSs (Figure S8, Supporting Information). The excellent rate capability and fast kinetics of 3DNG/TiN cathode may partially result from the high conductivity of TiN nanowires, which is further confirmed by the electrical conductivity test enabled by a single nanowire device setup (Figure S9, Supporting Information). The electrical conductivity of the TiN nanowire was calculated to be 4.0×10^4 S m^{-1}, which is almost 8000 times higher than that of the TiO_2 nanowire (5.2 S m^{-1}). The addition of highly conductive TiN can greatly improve the electrical conductivity of 3DNG/TiN composite. The electrical conductivity of the uncompressed 3DNG/TiN composite aerogel is 1.56 S m^{-1}, which is higher than that of 3DG/TiO_2 (0.47 S m^{-1}) and 3DNG (0.82 S m^{-1}). Therefore, the electrons involved in the charge and discharge processes can transport very fast in the network of the 3DNG/TiN cathode, which is favorable for the fast polysulfide conversion. To further investigate the stability of the 3DNG/TiN cathode, we tested the cell at 1 C for a long term (Figure 3e). An initial high capacity of 1480 mAh g^{-1} is obtained and the final capacity is 957 mAh g^{-1} (200 cycles). On the contrary, the 3DNG/TiO_2 and 3DNG cathodes show the initial capacity of 1178 and 1300 mAh g^{-1}, and only 681 and 554 mAh g^{-1} are remained after 200 cycles, respectively. All of the results are suggesting that the high conductivity and good stability of the 3DNG/TiN cathode are due to the stable 3DNG framework and the strong chemical interaction between the LiPSs and TiN nanowires.

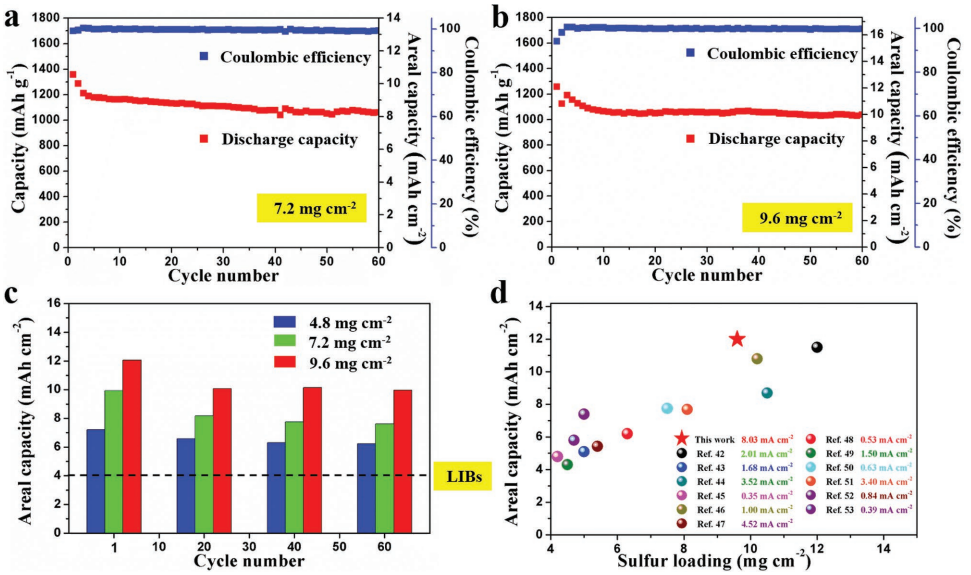

Figure 4. a,b) Cycling performance and the corresponding Coulombic efficiency of the 3DNG/TiN cathode with 7.2 mg cm^{-2} (a), and 9.6 mg cm^{-2} (b) sulfur loadings. c) Areal capacities of the three electrodes with different sulfur loadings at different cycles. d) Comparison of initial areal capacity of this work with that of Li–S batteries from recent publications which cycled more than 50 times and the sulfur loadings higher than 4 mg cm^{-2}.

In order to fully utilize the advantage of high theoretical capacity of the Li–S battery, the high areal sulfur loading is a critical factor for achieving the practical applications of Li–S batteries.[37–40] However, the higher loading of the insulating sulfur inevitably leads to much more severe shuttling of LiPSs and lower utilization of sulfur, meaning faster capacity decay and lower specific capacities. Therefore, optimizing the performance of Li–S batteries with a high sulfur loading still remains a big challenge. Previous studies have reported that only batteries with an areal capacity of higher than 4 mAh cm^{-2} can surpass the commercial LIBs.[41] In addition, considering the lower voltage of Li–S batteries than that of LIBs, even higher areal capacity is needed. In this work, with the sulfur loading of 4.8 mg cm^{-2}, 3DNG/TiN cathode already achieves an areal capacity of over 7 mAh cm^{-2}. In order to further verify the superiority of the 3DNG/TiN cathode, the batteries with higher sulfur loadings of 7.2 and 9.6 mg cm^{-2} were cycled at 0.5 C (**Figure 4**a,b). The high initial areal capacity of 9.94 mAh cm^{-2} was obtained with the sulfur loading of 7.2 mg cm^{-2}, and 8.2 mAh cm^{-2} was remained after 60 cycles. Furthermore, even with the very high sulfur loading of 9.6 mg cm^{-2}, 3DNG/TiN cathode delivered an ultrahigh areal capacity of 12.0 mAh cm^{-2} and 9.96 mAh cm^{-2} was remained after 60 cycles. Noticeably, the current density was calculated to be as high as 8.03 mA cm^{-2}. Figure 4c summarized the areal capacities of batteries with different sulfur loadings, clearly demonstrating that all these values are much higher than those of commercial LIBs (4.0 mAh cm^{-2}).[28] To illustrate the significance and importance of this work, we compared the capacities of related TMNs-based cathodes used in Li–S batteries (Table S1, Supporting Information), as well as the areal capacities of recently published high-sulfur-loading studies (Table S2, Supporting Information and Figure 4d). According to the data in the tables, the 3DNG/TiN cathode in the present study has the highest capacity and excellent rate performance compared to other TMNs cathodes. In addition, the 3DNG/TiN cathode also delivered higher areal capacity than the cathode materials in recent literature with a high sulfur loading.[42–53] It is worth noting that this remarkable performance is realized at a high current density of 8.03 mA cm^{-2}. As far as we know, this performance of the 3DNG/TiN cathode in our work is superior to the majority of the cathode materials in the reports on Li–S batteries in terms of sulfur loading and electrochemical performance, and it indeed provides the prospect of high-sulfur-loading Li–S batteries with fast charge and discharge capability and high power density.

In order to fully understand the interaction between the sulfur species and the host 3DNG/TiN, we conducted a series of characterizations of the 3DNG/TiN after 100 cycles at 0.5 C. The morphology of the 3DNG/TiN was well maintained after cycling and no aggregation of TiN nanowires was observed (**Figure 5**a,b). The typical elemental mappings of Ti, N, C, O, and S (Figure S10a–f, Supporting Information) clearly illustrated their homogeneous distribution in the 3DNG/TiN framework and the corresponding EDS showed that a much strong peak of sulfur appeared after cycling compared with that of the initial 3DNG/TiN (Figure S10g,h, Supporting Information). Moreover, the TEM mappings of the Ti, N, and S elements of a single TiN nanowire after cycling are shown in Figure 5c, this result provides the direct evidence for the strong chemical adsorption of LiPSs on the surface of TiN nanowire. The N1s peak for the TiN shifts to a higher binding energy after cycling, which may be ascribed to the new S–N–Ti interaction.[28] This should be ascribed to the electronegativity and polar of nitrogen which helps to form covalent bonding with sulfur species.[28,30] The Ti 2p peaks for TiN also displayed a major change after cycling. A new peak at 456.6 eV appeared (Figure 5e), which could be assigned to N–Ti–S bonding resulting from the interaction between TiN and LiPSs.[54,55]

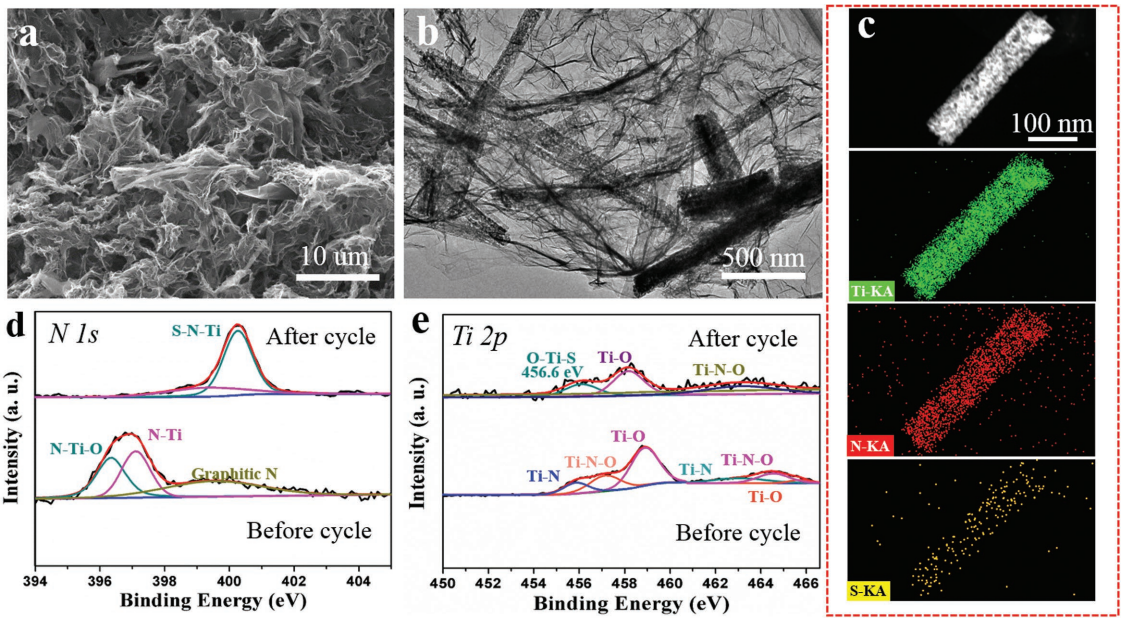

Figure 5. Morphology and structural characterization of the 3DNG/TiN after cycling at 0.5C for 100 cycles. a) SEM image, b) TEM image, c) TEM elemental mapping images, d,e) High-resolution N1s and Ti2p XPS spectrum, respectively.

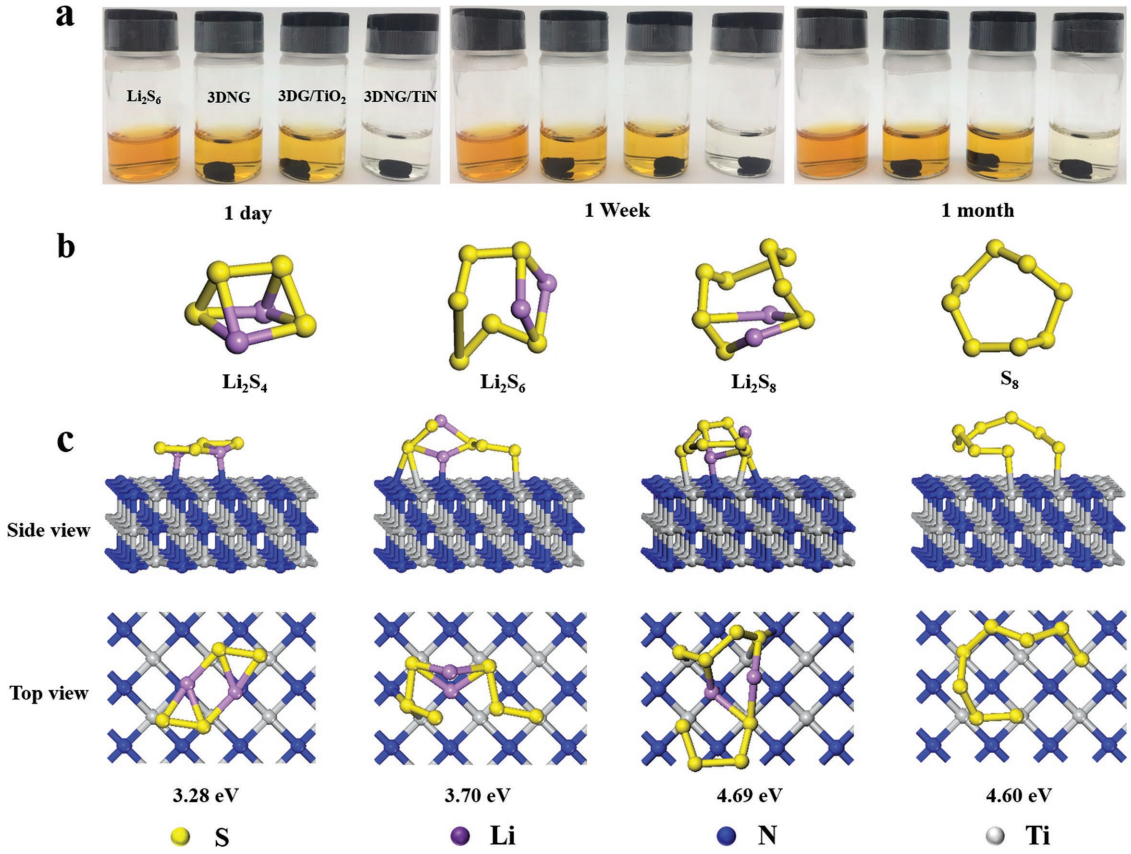

Figure 6. Adsorption test and the theoretical DFT calculation of 3DNG/TiN with Li_2S_n/S_8. a) Optical photograph of the Li_2S_6 and sulfur trapping by 3DNG/TiN, 3DG/TiO_2, and 3DNG, b) DFT-calculated molecular structures of Li_2S_n and S_8, and c) optimized configurations for the binding of Li_2S_n and S_8 to the TiN (200).

Figure 6a exhibits the camera images of the adsorption test using 3DNG, 3DG/TiO_2, and 3DNG/TiN with the 0.005 M Li_2S_6 solution. It is clear that after one day, the color of the solution containing 3DNG/TiN was almost colorless while the other samples still remained yellow. Moreover, after one week and even one month of the static adsorption tests, the color of the 3DNG/TiN-containing solution was still much lighter than the other two samples. The corresponding ultraviolet/visible absorption measurement was also carried out to investigate the Li_2S_6 adsorption effect of 3DNG, 3DG/TiO_2, and 3DNG/TiN (Figure S11, Supporting Information). It can be clearly seen that the absorption peak of Li_2S_6 in the visible light range obviously disappeared after adding 3DNG/TiN, indicating a better Li_2S_6 adsorption capability of 3DNG/TiN. To further reveal how the TiN adsorb LiPSs by forming strong chemical bonding, we elucidated the interaction between long-chain Li_2S_n (n = 4, 6, 8)/S_8 and TiN using density functional theory (DFT) calculations. The binding energies (E_b) of Li_2S_n/S_8 (molecular structures are shown in Figure 6b) with NG, TiO_2, and TiN were obtained by a CASTEP simulation package in the framework of DFT. In the adsorption structure (Figure 6c), the most favorable binding sites of Li_2S_n/S_8 are Li atoms which tend to bond with the N atoms, while sulfur can bond with both the N and Ti atoms on TiN (200), in which the S–N distance is 2.12 Å. While bonding with Ti on TiN, the S–Ti distance is 2.36 Å. DFT calculations confirm the strong interactions between LPSs with TiN and it is mainly owing to the bonding between Li/S and Ti/N. The E_b of Li_2S_4, Li_2S_6, Li_2S_8, and S_8 on TiN (200) surfaces are 3.28, 3.70, 4.69, and 4.60 eV, respectively. On the other hand, the corresponding adsorption energies of Li_2S_4, Li_2S_6, Li_2S_8, and S_8 on NG and TiO_2 surfaces are 0.35, 0.51, 0.63, 1.5 eV and 1.25, 1.66, 2.25, 2.16 eV, respectively (Figures S12 and S13, Supporting Information). According to the definition, a higher binding energy of TiN to LiPSs indicates a more energetically favorable interaction and stronger chemical anchoring of soluble LiPSs, which greatly contributes to the enhanced battery performance.

In conclusion, we employed a facile and effective method for the successful preparation of the 3DNG/TiN composite, combining porous 3DNG networks with highly conductive, polar TiN nanowires. This unique structure not only greatly increases the electrical conductivity of the electrode, but also effectively inhibits the shuttle effects due to the strong chemical adsorption of LiPSs by TiN, which can significantly enhance the cycle stability and rate performance of the Li–S battery. More importantly, this 3DNG/TiN architecture accommodated the high sulfur mass loading of 9.6 mg cm^{-2}, and showed an excellent electrochemical performance in Li–S cells. The final DFT calculations demonstrate that the inherent strong interaction between LiPSs/S_8 with TiN is the key factor to suppress the shuttle effects of LiPSs. This study will indeed give the bright prospect that high energy density and high power density can be achieved simultaneously for Li–S batteries.

Supporting Information

Supporting Information is available from the Wiley Online Library or from the author.

Acknowledgements

Z.L. and Q.H. contributed equally to this work. This work was supported by the National Natural Science Fund for Distinguished Young Scholars (51425204), the National Natural Science Foundation of China (51521001, 51832004, 51702247), the National Key Research and Development Program of China (2016YFA0202603), the Programme of Introducing Talents of Discipline to Universities (B17034), the Yellow Crane Talent (Science & Technology) Program of Wuhan City, the Fundamental Research Funds for the Central Universities (WUT: 2017III030, 2018IVB034, 2018IVA088, 2018III025) and the Basic Research Expense of The State Key Laboratory (20131d0005).

Conflict of Interest

The authors declare no conflict of interest.

Keywords

chemical anchoring, high areal capacity, lithium–sulfur batteries, TiN nanowires

Received: June 27, 2018
Revised: August 14, 2018
Published online:

[1] X. L. Ji, K. T. Lee, L. F. Nazar, *Nat. Mater.* **2009**, *8*, 500.
[2] P. G. Bruce, S. A. Freunberger, L. J. Hardwick, J. M. Tarascon, *Nat. Mater.* **2012**, *11*, 19.
[3] L. Sun, D. T. Wang, Y. F. Luo, K Wang, W. B. Kong, Y. Wu, L. N. Zhang, K. L. Jiang, Q. Q. Li, Y. H. Zhang, J. P. Wang, S. S. Fan, *ACS Nano* **2016**, *10*, 1300.
[4] L. F. Nazar, M. Cuisinier, Q. Pang, *MRS Bull.* **2014**, *39*, 436.
[5] M. R. Wang, G. X. Liu, H. Q. Wang, H. Z. Zhang, X. F. Li, H. M. Zhang, *J. Mater. Chem. A* **2018**, *6*, 7639.
[6] L. W. Ji, M. M. Rao, H. M. Zheng, L. Zhang, Y. C. Li, W. H. Duan, J. H. Guo, E. J. Cairns, Y. G. Zhang, *J. Am. Chem. Soc.* **2011**, *133*, 18522.
[7] H. L. Wang, Y. Yang, Y. Y. Liang, J. T. Robinson, Y. G. Li, A. Jackson, Y. Cui, H. J. Dai, *Nano Lett.* **2011**, *11*, 2644.
[8] Q. Zhao, X. F. Hu, K. Zhang, N. Zhang, Y. X. Hu, J. Chen, *Nano Lett.* **2015**, *15*, 721.
[9] P. T. Xiao, F. X. Bu, G. H. Yang, Y. Zhang, Y. X. Xu, *Adv. Mater.* **2017**, *29*, 1703324.
[10] Z. Li, L. X. Yuan, Z. Q. Yi, Y. M. Sun, Y. Liu, Y. Jiang, Y. Shen, Y. Xin, Z. L. Zhang, Y. H. Huang, *Adv. Energy Mater.* **2014**, *4*, 1301473.
[11] F. X. Wu, J. T. Lee, E. Zhao, B. Zhang, G. Yushin, *ACS Nano* **2016**, *10*, 1333.
[12] F. Pei, T. H. An, J. Zang, X. J. Zhao, X. L. Fang, M. S. Zheng, Q. F. Dong, N. F. Zheng, *Adv. Energy Mater.* **2016**, *6*, 1502539.
[13] G. X. Li, J. H. Sun, W. P. Hou, S. D. Jiang, Y. Huang, J. X. Geng, *Nat. Commun.* **2016**, *7*, 10601.
[14] X. Yang, L. Zhang, F. Zhang, Y. Huang, Y. S. Chen, *ACS Nano* **2014**, *8*, 5208.
[15] G. M. Zhou, H. Z. Tian, Y. Jin, X. Y. Tao, B. F. Liu, R. F. Zhang, Z. W. Seh, D. Zhuo, Y. Y. Liu, J. Sun, J. Zhao, C. X. Zu, D. S. Wu, Q. F. Zhang, Y. Cui, *Proc. Natl. Acad. Sci. USA* **2017**, *114*, 840.
[16] W. Z. Bao, D. W. Su, W. X. Zhang, X. Guo, G. X. Wang, *Adv. Funct. Mater.* **2016**, *26*, 8746.
[17] D. W. Su, M. Cortie, G. X. Wang, *Adv. Energy Mater.* **2017**, *7*, 1602014.

[18] X. Liu, J. Q. Huang, Q. Zhang, L. Q. Mai, *Adv. Mater.* **2017**, *29*, 1601759.
[19] T. H. Zhou, W. Lv, J. Li, G. M. Zhou, Y. Zhao, S. X. Fan, B. L. Liu, B. H. Li, F. Y. Kang, Q. H. Yang, *Energy Environ. Sci.* **2017**, *10*, 1694.
[20] X. Liang, C. Y. Kwok, F. Lodi-Marzano, Q. Pang, M. Cuisinier, H. Huang, C. J. Hart, D. Houtarde, K. Kaup, H. Sommer, T. Brezesinski, J. Janek, L. F. Nazar, *Adv. Energy Mater.* **2016**, *6*, 1501636.
[21] S. Z. Wei, W. Y. Li, J. J. Cha, G. Y. Zheng, Y. Yang, M. T. McDowell, P. C. Hsu, Y. Cui, *Nat. Commun.* **2013**, *4*, 1331.
[22] X. Liang, L. F. Nazar, *ACS Nano* **2016**, *10*, 4192.
[23] D. Zhao, Z. T. Cui, S. G. Wang, J. W. Qin, M. H. Cao, *J. Mater. Chem. A* **2016**, *4*, 7914.
[24] D. R. Deng, F. Xue, Y. J. Jia, J. C. Ye, C. D. Bai, M. S. Zheng, Q. F. Dong, *ACS Nano* **2017**, *11*, 6031.
[25] C. C. Li, J. J. Shi, L. Zhu, Y. Y. Zhao, J. Lu, L. Q. Xu, *Nano Res.* **2018**, *12*, 1.
[26] X. L. Li, R. W. Tang, K. Hu, L. Y. Zhang, Z. Q. Ding, *Electrochim. Acta* **2016**, *210*, 734.
[27] Z. H. Sun, J. Q. Zhang, L. C. Yin, G. J. Hu, R. P. Fang, H. M. Cheng, F. Li, *Nat. Commun.* **2017**, *8*, 14627.
[28] Z. M. Cui, C. X. Zu, W. D. Zhou, A. Manthiram, J. B. Goodenough, *Adv. Mater.* **2016**, *28*, 6926.
[29] T. G. Jeong, D. S. Choi, H. Song, J. Choi, S. A. Park, S. H. Oh, H. Kim, Y. Jung, Y. T. Kim, *ACS Energy Lett.* **2017**, *2*, 327.
[30] Z. X. Hao, L. X. Yuan, C. J. Chen, J. W. Xiang, Y. Y. Li, Z. M. Huang, P. Hu, Y. H. Huang, *J. Mater. Chem. A* **2016**, *4*, 17711.
[31] N. Mosavati, V. R. Chitturi, S. O. Salley, K. Y. Simon Ng, *J. Power Sources* **2016**, *321*, 87.
[32] M. Wang, Q. H. Liang, J. W. Han, Y. T, D. H. Liu, C. Zhang, W. Lv, Q. H. Yang, *Nano Res.* **2018**, *11*, 3480.
[33] W. D. Zeng, Z. Wang, M. M. C. Cheng, K. Y. Simon Ng, *J. Electrochem. Soc.* **2018**, *165*, A1011.
[34] M. Sluban, P. Umek, Z. Jagličić, J. Buh, P. Smitek, A. Mrzel, C. Bittencourt, P. Guttmann, M. H. Delville, D. Mihailović, *ACS Nano* **2015**, *9*, 10133.
[35] C. Barchasz, F. Molton, C. Duboc, J. C. Lepretre, S. Patoux, F. Alloin, *Anal. Chem.* **2012**, *84*, 3973.
[36] Y. X. Yin, S. Xin, Y. G. Guo, L. J. Wan, *Angew. Chem., Int. Ed.* **2013**, *52*, 13186.
[37] H. J. Peng, J. Q. Huang, X. B. Cheng, Q. Zhang, *Adv. Energy Mater.* **2017**, *7*, 1700260.
[38] S. H. Chung, C. H. Chang, A. Manthiram, *ACS Nano* **2016**, *10*, 10462.
[39] R. P. Fang, S. Y. Zhao, P. X. Hou, M. Cheng, S. G. Wang, H. M. Cheng, C. Liu, F. Li, *Adv. Mater.* **2016**, *28*, 3374.
[40] L. Liu, A. Manthiram, *ACS Energy Lett.* **2017**, *2*, 2205.
[41] J. X. Song, T. Xu, M. L. Gordin, P. Y. Zhu, D. P. Lv, Y. B. Jiang, Y. S. Chen, Y. H. Duan, D. H. Wang, *Adv. Funct. Mater.* **2014**, *24*, 1243.
[42] S. H. Chung, L. Liu, A. Manthiram, *ACS Energy Lett.* **2018**, *3*, 568.
[43] X. Y. Zhu, W. Zhao, Y. Z. Song, Q. C. Li, F. Ding, J. Y. Sun, L. Zhang, Z. F. Liu, *Adv. Energy Mater.* **2018**, *8*, 1800201.
[44] C. H. Chang, A. Manthiram, *ACS Energy Lett.* **2018**, *3*, 72.
[45] Q. Zhao, Q. Z. Zhu, J. W. Miao, Z. R. X. Guan, H. Liu, R. J. Chen, Y. B. An, F. Wu, B. Xu, *ACS Appl. Mater. Interfaces* **2018**, *10*, 10882.
[46] Q. Pang, X. Liang, C. Y. Kwok, J. Kulisch, L. F. Nazar, *Adv. Energy Mater.* **2017**, *7*, 1601630.
[47] L. B. Ma, H. Yuan, W. J. Zhang, G. Y. Zhu, Y. R. Wang, Y. Hu, P. Y. Zhao, R. P. Chen, T. Chen, J. Liu, Z. Zhu, Z. Jin, *Nano Lett.* **2017**, *17*, 7839.
[48] Z. Yuan, H. J. Peng, J. Q. Huang, X. Y. Liu, D. W. Wang, X. B. Cheng, Q. Zhang, *Adv. Funct. Mater.* **2014**, *24*, 6244.
[49] Q. Pang, D. Kundu, L. F. Nazar, *Mater. Horiz.* **2016**, *3*, 130.
[50] Y. J. Li, J. M. Fan, J. H. Zhang, J. F. Yang, R. M. Yuan, J. Chang, M. S. Zheng, Q. F. Dong, *ACS Nano* **2017**, *11*, 11417.
[51] M. P. Yu, J. S. Ma, M. Xie, H. Q. Song, F. Y. Tian, S. S. Xu, Y. Zhou, B. Li, D. Wu, H. Qiu, R. M. Wang, *Adv. Energy Mater.* **2017**, *7*, 1602347.
[52] J. X. Song, M. L. Gordin, X. Terrence, S. Chen, Z. X. Yu, H. Sohn, J. Lu, Y. Ren, Y. H. Duan, D. H. Wang, *Angew. Chem., Int. Ed.* **2015**, *54*, 4325.
[53] P. Lv, J. M. Zheng, Q. Y. Li, X. Xie, S. Ferrara, Z. M. Nie, L. B. Mehdi, N. D. Browning, J. G. Zhang, G. L. Graf, J. Liu, J. Xiao, *Adv. Energy Mater.* **2015**, *5*, 1402290.
[54] Z. B. Xiao, Z. Yang, L. Wang, H. G. Nie, M. Zhong, Q. Q. Lai, X. J. Xu, L. J. Zhang, S. M. Huang, *Adv. Mater.* **2015**, *27*, 2891.
[55] Z. Liang, G. Y. Zheng, W. Y. Li, Z. W. Seh, H. B. Yao, K. Yan, D. S. Kong, Y. Cui, *ACS Nano* **2014**, *8*, 5249.